HHS Public Access

Author manuscript

J Mech Behav Biomed Mater. Author manuscript; available in PMC 2022 April 19.

Published in final edited form as:

J Mech Behav Biomed Mater. 2020 October ; 110: 103956. doi:10.1016/j.jmbbm.2020.103956.

Investigating the birth-related caudal maternal pelvic floor muscle injury:

The consequences of low cycle fatigue damage

Maria C.P. Vila Pouca[1,2], **Marco P.L. Parente**[1,2], **Renato M. Natal Jorge**[1,2], **James A. Ashton-Miller**[3]

[1]Department of Mechanical Engineering, Faculty of Engineering of University of Porto, Porto, Portugal

[2]Institute of Science and Innovation in Mechanical and Industrial Engineering, Porto, Portugal

[3]Departments of Mechanical and Biomedical Engineering, College of Engineering and School of Kinesiology, University of Michigan, Ann Arbor, Michigan, USA

Abstract

Background: One of the major causes of pelvic organ prolapse is pelvic muscle injury sustained during a vaginal delivery. The most common site of this injury is where the pubovisceral muscle takes origin from the pubic bone. We hypothesized that it is possible for low-cycle material fatigue to occur at the origin of the pubovisceral muscle under the large repetitive loads associated with pushing during the second stage of a difficult labor.

Purpose: The main goal was to test if the origin of the pubovisceral muscle accumulates material damage under sub-maximal cyclic tensile loading and identify any microscopic evidence of such damage.

Methods: Twenty origins of the ishiococcygeous muscle (homologous to the pubovisceral muscle in women) were dissected from female sheep pelvises. Four specimens were stretched to failure to characterize the failure properties of the specimens. Thirteen specimens were then subjected to relaxation and subsequent fatigue tests, while three specimens remained as untested controls. Histology was performed to check for microscopic damage accumulation.

Results: The fatigue stress-time curves showed continuous stress softening, a sign of material damage accumulation. Histology confirmed the presence of accumulated microdamage in the form of kinked muscle fibers and muscle fiber disruption in the areas with higher deformation, namely in the muscle near the musculotendinous junction.

Conclusions: The origin of ovine ishiococcygeous muscle can accumulate damage under sub-maximal repetitive loading. The damage appears in the muscle near the musculotendinous junction and was sufficient to negatively affect the macroscopic mechanical properties of the specimens.

Keywords

fatigue; pelvic muscle injury; microscopic damage; pubovisceral muscle; histology; tissue fatigue damage

1. Introduction

Pelvic organ prolapse, a serious and common condition, adversely affects quality of life, particularly in older women[18,29,55]. The lifetime risk of needing prolapse surgery ranges between 1 in 10 to 1 in 5 women, with over 300, 000 surgeries being performed for this condition in the U.S. every year[17,53]. Unfortunately, the surgery has a failure rate of approximately 30% [4], so preventing prolapse in the first place would be desirable. To that end, mechanistic insights are needed into the injury mechanism(s). Pelvic floor muscle injury occurs most frequently during the first vaginal birth and has been identified as one of the major causes for pelvic organ prolapse [30,45]. Moreover, a characteristic site of injury has been identified with magnetic resonance imaging to be the origin of the pubovisceral muscle from the pubic bone[12–14,34].

Most muscles originate from bone via a tendon or an aponeurosis that itself interdigitates with muscle fibers and fascicles called the musculotendinous junction (MTJ), with their other end inserting onto a bone at an enthesis where the tendon/aponeurosis inserts into the bone [47,50]. Injuries to bone-tendon/aponeurosis-muscle units are common and tend to occur at the tendon/aponeurosis-bone junction or at the musculotendinous junction [47]. From a mechanical point of view, junctions between dissimilar materials are well known to be regions of mechanical stress concentration, not only due to the different material properties, but also because these regions are usually accompanied by a change in cross-sectional area; this means that if the whole unit is uniformly loaded these junctions have to sustain higher stresses, making them more prone to tear [50]. In the human, the pubovisceral muscle originates bilaterally from the dorsal aspect of the pubic bone via an aponeurosis on either side of the pubic symphysis[26,27].

Low cycle fatigue failure can occur in soft connective tissues. For example, sub-maximal repetitive loading has been demonstrated to cause failure of the origin of the human anterior cruciate ligament (ACL), a highly organized connective tissue structure within the knee, in less than 100 loading cycles [33]. Recently, Chen *et al.* [9] found molecular, cellular and ultrastructural evidence of low-cycle fatigue damage accumulation at the origin of the ACL, more specifically at its femoral enthesis, following cyclic sub-maximal loading. So, if low-cycle material fatigue can occur at the origin of the ACL, we reasoned that low-cycle material fatigue could also occur at the origin of the pubovisceral muscle during the second stage of a difficult vaginal delivery, when it can be stretched to at least 3 times its original length every 3 min over a 3 h period [32,41]. The concept of low cycle material fatigue is that a structure can fail under two or more repetitive sub-maximal loading cycles that would not, by themselves, cause failure. This occurs because in each loading cycle there is a microscopic damage accumulation that weakens the structure, making it more prone to fail with the increase of damage accumulation.

At the origin of the ACL the damage accumulation occurs at the femoral enthesis, the ligament-bone junction, and the ligament, as in tendon, consists primarily of collagen type I[3,54]. Moreover, there are a considerable number of studies that have shown fatigue damage accumulation in tendons and collagenous structures at the fiber and fibril level [5,16,46,48,51,52,56]. With these considerations our working hypothesis was that the origin of

the pubovisceral muscle could accumulate microscopic damage at the tendon-bone interface under repetitive sub-maximal loading with the number of loading cycles being equivalent to that experienced during a difficult vaginal delivery. Our alternative hypotheses were that damage accumulation could occur in a different site, or that no evidence of fatigue damage accumulation would occur.

To test our hypothesis, we performed low-cycle fatigue tests on ovine specimens using a test protocol of 60 cycles to 60% failure displacement and analyzed the behavior of the stretch-stress curves. We also examined histological sections of the specimens in a search for evidence of damage accumulation. The tests were performed on the origin of the ishiococcygeous muscle from female mature sheep, which is the structure most analogous to the origin of the pubovisceral muscle in women.

Once we had obtained the mechanical properties of the ishiococcygeous muscle origin, we developed a constitutive model for fatigue damage that was incorporated into a visco-hyperelastic material model. Using a micro-genetic algorithm, we calibrated the material parameters for the averaged response of the stress-time curve of our fatigue tests. This is important for the development of realistic finite element models, which are highly dependent on defining the appropriate constitutive laws and also defining the appropriate material parameters [8]. Finally, to explore how the results might apply to humans, we developed a simplified finite element model of the origin of the pubovisceral muscle using our visco-hyperelastic material model that included fatigue damage.

2. Materials and methods

2.1 Animal model of the origin of the pubovisceral muscle

While there is no perfect substitute for human specimens, using animal models in research has become a common alternative since they provide significantly improved access to tissue and there are fewer ethical constraints[2,11].

In this study we decided to choose sheep as an animal model for the origin of the pubovisceral muscle. This choice was made because they represent an established reproductive model for humans, have prolonged labor with relatively large fetuses, spontaneously develop prolapse, have similar pelvic muscles anatomy and were more available than other large models such as primate[2].

The human pelvic floor muscles, or levator ani, can be subdivided in the puborectal, pubovisceral (also known as pubococcygeal) and iliococcygeus muscles. The human pubovisceral muscle originates from the pubic bone on either side of the pubic symphysis and inserts into the perineal body, vaginal wall and the anal canal [25]. In sheep, the levator ani appears as a uniform muscle [6,49], and is designated as the ishiococcygeous if one follows the terminology of Basset, E.G [6]. Our dissections confirmed that the ovine ishiococcygeous originates from the ishium and fans out from the origin to insert into the vaginal wall, anal canal and tail bones (Figure 1b), consistent with Basset, E.G. [6] (Figure 1a). Although there are some dissimilarities, we conclude that the origin of the ovine ishiococcygeous muscle is the most homologous structure to the origin of the pubovisceral muscle in humans.

2.2 Specimens procurement and preparation

Ten pelvises from female skeletally mature nulliparous sheep were collected thereby providing 20 specimens of the origin of pubovisceral muscle. Age and weight were provided for eight pelvises and the longitudinal and cross-sectional dimensions of the pelvic cavity were measured for all specimens. The breed of the animals was not provided. Two fresh pelvises, obtained from the Michigan State University Meat laboratory, were double bagged and stored in the Biomechanics Research Lab at the University of Michigan at –20ºC. Eight pelvises were provided by the University of Minnesota's Experimental Surgical Services and sent to the University of Michigan via dry ice shipments.

The pelvises were kept frozen at –20ºC for between 3 and 68 days (mean 28 ± 16 days). Each pelvis was thawed in their bags to room temperature overnight for dissection the next day. After mostly blunt dissection was used to identify the ischococcygeal muscle, a scalpel was used to free the insertions of the muscle at the vagina, anal canal and coccygeal bone. The ischocyccygeal muscle takes origin immediately posterior to the obturator foramen from the posteromedial aspect of the inferior ischium at its junction with the pubic bone. So the muscle origin and underlying bone were excised *en bloc* from the adjacent pelvic bone by using a bone saw and pruning shears to divide the ischia ventral to the origin and the pubic bone posterior to the origin (Figure 1). The paired left and right pubovisceral specimens were then kept in a sealed container in a refrigerator for the mechanical tests to be performed the following day. Prior to the mechanical tests, the specimens were thawed to room temperature. A 1x Phosphate-buffered saline (PBS) was used to fully hydrate the tissues. Then, to avoid a muscle tear caused by grips, the distal end of the muscle specimen was adhered between two pieces of ripstop nylon (64 gsm) using cyanoacrylate glue. In all the specimens, the ripstop ended 15 mm from the MTJ. To ensure a proper grip at the bone end of the specimen, the bone was trimmed and flattened using a DREMEL® equipped with a flush cut blade. During the preparation, the specimens were kept hydrated by frequently spraying PBS solution or keeping them covered with a Kimwipe soaked in 1x PBS. Figure 2 shows a specimen prior to the mechanical test, before and after preparation with a digital caliper showing the scale in mm. Specimens were designated '1' through '10' according to each pelvis, with an 'L' or 'R' for left or right origin, respectively. So, a reference to specimen '1R' and '1L' means they both belong to the same pelvis (No. 1) and are the right and left ishiococcygeous origin, respectively.

2.3 Experimental design and protocol

This study was divided in two parts. In the first part, ultimate tensile tests were performed, to characterize the failure mechanical properties of the muscle-tendon-bone unit. In the second part, relaxations and fatigue tests were performed respectively at 35% and 60% of the failure displacement. Three specimens were used for the ultimate tensile tests and 16 specimens for relaxation and fatigue tests. Of these 16 specimens, 3 samples were not tested in order to remain as untested controls. One specimen was discarded due to tear at the grips during the ultimate tensile test. The controls were randomly selected from among the 16 specimens using a custom Matlab® program.

Custom design clamps were chosen to grip the specimens, however, to completely avoid slippage, an abrasive sandpaper was also glued via double-sided adhesive tape to each grip. The sandpaper made direct contact proximally with the bone, and for the other grip contact with the ripstop nylon. An ADMET eXpert 4500 MicroTest system (Resolution 0.001N) with MTESTQuattro (version 5) controller and a 100 lbf load cell (WMC-100, Interface) was the equipment used for all the tests. Figure 3 shows the specimen inserted in the setup and ready for testing.

The ultimate tensile tests were performed under displacement control while the specimens were stretched to failure at a displacement rate of 0.1 mm/s. It was decided not to precondition the specimens since it changes the stress-strain response of the tissues [10]. Force-displacement data were acquired at a rate of 0.5 s^{-1}. Failure properties were obtained at the peak of the force displacement curve: the mean force to failure and mean displacement to failure were calculated from the results of all samples. The mean displacement to failure served as the failure 'baseline' for the relaxation and fatigue tests.

The relaxation and fatigue tests were performed under displacement control. For the relaxation tests, the specimens were stretched up to 35% failure displacement at 10 mm/s and then the same displacement was maintained for 1000 s. Force-displacement data were acquired at 0.01 s^{-1} during the first 10 seconds, at 0.1 s^{-1} between 10 and 100 sec, and at 1 s^{-1} for the remaining 900 seconds. At the end of the relaxation test the specimen was taken back to the initial position and allowed to rest for 20 min in the setup. Then, the fatigue test was carried out. A preload of 0.7 N was initially applied to take up the slight slack caused by the relaxation test. The specimen was then cyclically stretched between 60% and 45% of the failure displacement for 60 cycles at a rate of 0.1 mm/s. This is approximately one loading-unloading cycle every 53 s resulting in a fatigue test with a duration of 53 min. This duration corresponds with the mean length of a second stage of labor of 54.4 ± 23.6 min [28]. The 60% failure displacement was chosen because during vaginal birth the levator ani hiatus has an estimated stretch ratio of 1.62–3.76 [23] and we wanted to stretch the specimens to a large deformation, but one that still lay in the sub-maximal range. Moreover, we predicted that the specimen would have permanent deformation so, to avoid compression in the unloading stage, we decided to unload to 45% failure displacement instead of unloading to the initial position. Force-displacement data were acquired at a rate of 1 s^{-1}. Two cameras Point Grey GRAS-50S5M-C acquired a picture per second during the test. Testing protocols are summarized in Table 1

Throughout the mechanical tests, the sample was kept hydrated by regularly spraying 1x PBS. Samples' initial cross-sectional area was assumed to be a rectangle and both the thickness and the width were measured at the MTJ using the digital caliper with a resolution of 0.01 mm. A minimum of three measurements were performed for each dimension. For the stress calculation, force was divided by initial and non-deformed cross-sectional area. So, throughout the manuscript, the plotted stresses are engineering stresses, also known as first Piola-Kirchhoff stresses, and represent force in the current configuration divided by area in the non-deformed reference configuration. The stretch can be defined as L_f/L_i, where L_f is the final and L_i the initial grip-to-grip distance.

2.4 Digital image correlation

Digital image correlation was used to track a speckle pattern on a sequence of images obtained from the fatigue tests in order to calculate the displacement or strain field on the surface of the specimen. To create the speckle pattern, one surface of the specimen was sprayed with graphite powder. which was applied with a squeeze bulb pump. The outlet had a net in order to sift through smaller and more consistent speckle sizes for use. Digital image correlation was performed using the software Vic-3D 7.

2.5 Permanent deformation

As referred in section 2.2, the distance from the MTJ to the ripstop nylon was originally set to 15 mm. After the fatigue tests, the same distance was remeasured using a digital caliper in all the specimens in order to provide an estimate of the permanent deformation due to the submaximal cyclic loading.

2.6 Microscopic damage assessment

A histological evaluation was performed to assess if there was damage accumulation in the specimens subjected to cyclic loading at a submaximal level. We were aware that the freeze/thaw process, to which all specimens were subjected to, can affect the appearance of the muscle's microscopic structure, with loss of striation, loss of intracellular staining and formation of ice crystals [19]. As such, the analysis between the controls and tested specimens was made with those artifacts in mind when assessing any true mechanical damage.

Due to the size of each sample it was necessary to divide it in two, one part including the muscle-tendon and the other, the tendon-bone (Figure 4) in order to fit within the histology slide cassettes. Tendon-muscle sections were again divided in two so that one part was sliced in the y-z plane and the other in the y-x plane (Figure 4). Tendon-bone sections were only sliced in the y-z plane. The specimens were fixed immediately after the fatigue test in 10% Formalin for 3–4 days. In the case of each control, the specimen was kept hydrated with 1xPBS during the testing phase of the contralateral specimen and both specimens were fixed at the same time.

After fixation, the samples were rinsed under running tap water for 20 min and then transferred to 70% Ethanol. The tendon-muscle samples were then ready for the paraffin processing procedure: 1 h in 80% ethanol, 2 h in 95% ethanol, 3 h in 100% ethanol, 3 h in xylene and 3 h in paraffin. Tendon-bone samples had to be decalcified using 20% EDTA, the decalcification being checked regularly using a FaxitronTMX-Ray Specimen Radiography System. After decalcification, the tendon-bone specimens were submitted to the same paraffin processing procedure as the tendon-muscle specimens. The next step was to embed the samples in paraffin, which was performed using a Leica HistoCore Arcadia embedding center. A Leica RM2255 microtome was then used to section 5 μm slices of all samples. Samples were stained with Masson's Trichrome and observed on a Nikon E800 light microscope. The Masson's Trichrome stain allowed us to distinguish between muscle cells and collagen fibers, which are stained red and blue, respectively. Cell nuclei stained black.

2.7 Constitutive modeling and finite element simulation

Based on our experimental evidence, presented in section 3.1-3.3, we assumed a transversely isotropic response and considered the viscoelastic behavior. We chose to apply and develop a phenomenological material model since they tend to have a simpler implementation, which makes them more robust and computationally efficient than the complex multi-scale models, and often conduct to similar macroscopic results. Multi-scale models have the advantage that the material parameters have generally a straightforward relationship to with structural features [35], however, depending the desired application they are not always necessary. Moreover, multi-scale models are computationally more expensive and tend to have a greater number of material parameters which complicate any real application. We considered the Holzapfel-Gasser-Ogden (HGO) [22] model for the hyperelastic behavior, paired with the generalized Maxwell-model for the viscous effects [20,21] and a phenomenological fatigue damage material model, whose law of evolution was developed in this work. So, the complete material model is transversely isotropic visco-hyperelastic, including a continuous damage model.

Since the high water content causes soft tissues to be incompressible or quasi-incompressible [35], we applied a penalty function for the volumetric contribution to assure incompressibility. The complete strain energy function can be represented in a decoupled form as:

$$\Psi = \Psi_{vol} + \left[(1 - D_m) \cdot \left(\overline{\Psi}_m + \overline{\Psi}_m^{vsc}\right)\right] + \left[(1 - D_f) \cdot \left(\overline{\Psi}_f + \overline{\Psi}_f^{vsc}\right)\right] \quad (1)$$

where Ψ_{vol} is the volumetric contribution, $\overline{\Psi}_m$ is the isochoric matrix contribution, $\overline{\Psi}_f$ the isochoric collagen fibers contribution, $\overline{\Psi}_m^{vsc}$ and $\overline{\Psi}_f^{vsc}$ are the viscous contributions associated respectively with the ground matrix and with the collagen fibers. $D_{*}(0 < D_{*} < 1\ {}_{*=m,f})$ are the continuous damage variables affecting each isochoric contribution of the strain energy. The index m, f refer respectively to the ground matrix and collagen fibers contributions or material parameters. The specific contributions can be defined as:

$$\Psi_{vol} = \kappa\left(\frac{J^2 - 1}{2} - \ln(J)\right) \quad (2)$$

$$\overline{\Psi}_m = C_{10}\left(\overline{I}_1 - 3\right) \quad (3)$$

$$\overline{\Psi}_f = \frac{k_1}{2k_2}\left\{\exp\left[\left(\overline{I}_4 - 1\right)^2\right] - 1\right\} \quad (4)$$

$$\overline{\Psi}_*^{vsc} = \sum_{\alpha=1}^{m} \gamma_{*\alpha}\left(\overline{\mathbf{C}}, \overline{\mathbf{\Gamma}}_\alpha\right)_{*\ =\ m,\ f} \quad (5)$$

where $J = \det \mathbf{F}$ is a measure of the volume variation, being $\mathbf{F}$ the deformation gradient. $\mathbf{C} = \mathbf{F}^T\mathbf{F}$ is the right Cauchy-Green deformation tensor and $\overline{C} = J^{-2/3}C$ is the isochoric right

Cauchy-Green deformation tensor, associated with the volume preserving deformation of the material. $\bar{I}_1 = (\overline{\mathbf{C}})$ is the first invariant of the of the isochoric Cauchy-Green tensor and $\bar{I}_4 = \bar{\lambda}_f^2 = \mathbf{m}_0 \cdot \overline{\mathbf{C}}\,\mathbf{m}_0$ is a pseudo-invariant arising directly from the anisotropy that is equal to the square of the stretch $\bar{\lambda}_f$ in the fiber direction $\mathbf{m}_0$. $\gamma_{\divideontimes\alpha}$ are scalar-valued functions that may be seen as a dissipative potential and $\overline{\mathbf{\Gamma}}_\alpha$ are tensorial variables, akin $\overline{\mathbf{C}}$, and characterize the viscoelastic isochoric response of the material. $\alpha = 1,2, \ldots m$ represents the number of viscoelastic processes, denoted by the number of parallel elements in the Maxwell model. Each Maxwell element can be represented by a spring in series with a dashpot. The spring represents the solid behavior and is characterized by a free energy parameter $\beta_{\divideontimes\alpha\ \divideontimes=m,f,}$ and the dashpot characterizes the viscous behavior and is function of a relaxation time $\tau_{\divideontimes\alpha\ \divideontimes=m,f}$. The material parameters of this constitutive model are: $C_{10.}$ for the ground matrix contribution, k_1 and. $K_{2,}$ for the fiber contribution, $\alpha = 1,2, \ldots m$, $\beta_{\divideontimes\alpha,\ \divideontimes=m,f}$ and $\tau_{\divideontimes\alpha\ \divideontimes=m,f,}$ for the viscous contribution and κ, which is the bulk modulus, for the volumetric contribution. Since we wanted to guarantee incompressibility, we defined the bulk modulus to a very high value, κ =100000, which was sufficient to guarantee that $J = 1$ and $\Psi_{vol} = 0$. More details concerning the transversely isotropic material model and the generalized Maxwell model for viscoelasticity can be found elsewhere [20–22].

The novelty of this constitutive model is the continuous damage model, which was developed using the concept of accumulated equivalent strain Ξ_t^{acc}, as defined by Peña, *et al* 2009 [42]. This allows for a continuous damage accumulation within the whole strain history of the deformation process [42]. It can be represented as:

$$\Xi_t^{acc} = \int_0^t \left| d\overline{\Psi}(\mathbf{C}) \Big/ ds \right| ds \tag{6}$$

Which gives a simple equation of evolution:

$$\frac{\mathrm{d}\Xi_t^{acc}}{\mathrm{dt}} = \left| \frac{\mathrm{d}\overline{\Psi}(\mathbf{C})}{dt} \right| \tag{7}$$

The damage propagation and accumulation was defined using a modification of Lemaitre and Plumtree nonlinear cumulative expression [39], in which the ratio between the number of cycles and the number of cycles to fatigue failure was replaced with the ratio between the accumulated equivalent strain and its maximum value. We also added a parameter, D_{max}, which allows one to control the weight of the damage variable. This parameter was added mostly due to numerical problems that often arise when performing a complex simulation with a damage material model. If the damage variable evolves to be equal to 1 in all the isochoric strain energy contributions, even if only in one finite element, the simulation stops since there is no stiffness in that finite element. This indicates that there is a tear in that region, but it can bring the simulation to an abrupt and early halt. To overcome this problem, we can now define the maximum amount of damage with the D_{max} parameter. Even if we are expecting a complete tear, we can set it to be almost equal to 1 and complete the simulation. In our case, we decided to be more conservative and set the maximum damage of

the ground matrix to 0.9, since no complete tear was observed in the specimens (see section 3).

$$D_{*} = D_{\max\ *}\left\{1 - \left(1 - \frac{\Xi_{t\ *}^{acc}}{\Xi_{\max\ *}^{acc}}\right)^{1/C_{*}}\right\}_{*\ =\ m,\,f} \tag{8}$$

The maximum value of the accumulated equivalent strain Ξ_{max}^{acc}, the exponent C and the weight parameter D_{max} ($0 < D_{max} \leq 1$) are the damage model material parameters.

One interesting aspect about this law of evolution is that despite its simplicity, we can consider a linear or nonlinear evolution just by controlling the parameter C. If C<1 the evolution is nonlinear and faster in the earlier deformation stages, for C=1 the evolution is linear, and for C>1 it is again nonlinear but slower in the initial deformation stages and faster closer to the tearing point. For this reason, it is a versatile damage law that can be applied to different materials.

The criteria for damage evolution can be represented as:

$$\dot{\Xi}_{t}^{acc} = \begin{cases} \dfrac{d\overline{\Psi}}{dt},\ \dot{\Xi}_{t}^{acc} \geq 0 \\ 0,\ \dot{\Xi}_{t}^{acc} < 0 \end{cases} \tag{9}$$

To calibrate the constitutive material parameters (with exception of $D_{max\ *}$), a micro-genetic algorithm was developed using MATLAB® integrated with Python and ABAQUS® finite element software. Succinctly, the micro-genetic algorithm generates randomly a micro population of nine elements. Afterwards, the fitness of each element is analyzed, and the fittest element is carried on to the next generation. The remaining elements go through a tournament selection strategy in which the winner elements become parents to the next generation. To develop the next generation, these parents suffer a crossover to create the elements of the next generation. After this, the convergence of the population is checked and if there is no diversity, the micro-population is restarted randomly, with exception of the fittest element, which is always carried to the next generation. In this work, the elements of the population were the constitutive model parameters and the fitness of each element was evaluated using a least squares evaluation function, F_e, between the experimental data and the solution from the numerical software ABAQUS®, in which our material model was implemented via user-defined subroutine UMAT:

$$F_e = \sqrt{\sum_{i=1}^{n} \frac{\left(P_i^e - P_i^{\Psi}\right)^2}{n-2}} \tag{10}$$

n is the number of considered experimental points and P_i^e and P_i^Ψ are respectively the engineering stresses in the direction of the applied stretch from the experimental data and from the numerical simulation in ABAQUS®.

The simulation was performed to replicate the experimental protocol of the fatigue experimental tests, including the 60 cycles and 3212 experimental points. The geometrical model used to calibrate the parameters is presented in Figure 5 and it is a simplification of our average specimen. Only 1/8 of the specimen was modelled since we applied symmetry boundary conditions. The mesh consists in 224 eight-node brick elements (C3D8). The bottom elements were clamped to simulate the grip in the experimental test. The fibers were assumed to have a principal direction, which was defined in the direction of the applied stretch. The variable used to compare with the experimental data was the engineering stress in the direction of the applied load. We decided to use an averaged response of all the finite elements in the geometrical model, since our experimental data corresponds also to an averaged response of the complete specimen. Since we calibrated the material parameters from all the contributions (hyperelastic, viscoelastic and damage) simultaneously, the constitutive model is able to capture the overall behavior, thereby overcoming the inconsistency that might occur with the Generalized Maxwell model for viscoelasticity [44].

To evaluate the fitting, we calculated the coefficient of determination and the absolute error mean. The coefficient of determination can be obtained as:

$$R^2 = 1 - \frac{S_{res}}{S_{tot}} \tag{11}$$

where $S_{res} = \sum_{i=1}^{n} \left(P_i^e - P_i^\Psi\right)^2$ is the sum of the squares of the residuals with the experimental data values and $S_{tot} = \sum_{i=1}^{n} \left(P_i^e - \overline{P_i^e}\right)^2$ is the total sum of squares, with the mean of the experimental data $\overline{P_i^e}$, and n is the number of data points.

The absolute error mean can be defined as:

$$\bar{r} = \frac{\sum_{i=1}^{n} \left|P_i^e - P_i^\Psi\right|}{n} \tag{12}$$

where $\sum_{i=1}^{n} \left|P_i^e - P_i^\Psi\right|$ is the sum of the absolute differences between the experimental data and the numerical values and n is the number of data points.

The coefficient of determination is widely used, and varies between 0 and 1, being 1 the optimal value. The mean absolute error allows to quantitatively analyze the differences and, when compared with the resolution of the experimental measurements, can also be a tool to test the fitting. In our work, since we are analyzing engineering stresses, the resolution can be obtained dividing the force resolution by the area resolution. According to the ADMET specifications, the force resolution is 0.001N, and due to the digital caliper used in the

area measurements, area resolution is 0.01mm^2. As such, the resolution of the engineering stresses is 0.1 MPa.

After calibrating the constitutive model parameters, we decided to use the finite element model to better understand the response of our specimen and its material properties. As presented in sections 3.2 and 3.3, the specimen has a visco-hyperelastic behavior and shows signs of material damage. As such, applying the same simulation used for calibrating the material parameters, we compare the response considering the complete constitutive model, with a response including only a viscoelastic behavior and including only the continuous damage model. This helps one understand the effect of each contribution.

3. Results

The longitudinal length (approximate distance between pubic symphysis and coccyx) and cross-sectional width (approximate distance between the obturators) were measured in all pelvises to be 11.85±1.86mm and 10.13±3.14mm, respectively. The weight and age of the sheep was provided in the 8 pelvises (16 specimen) used for the relaxation and fatigue tests and were 83.3±8.2Kg and 1 year 10 months±7 months, respectively.

The mean width of all the specimens at the MTJ was 14.89±2.63mm, the thickness was 3.07±0.57mm and the initial grip-to-grip distance 25.72±6.24mm.

3.1 Ultimate tensile tests

The average results of the force-displacement curve are illustrated in Figure 6a. Using the averaged response, the ultimate tensile displacement was 17.1±2.4mm and the ultimate tensile force 79.8±8.8N. Normalizing, the ultimate tensile stretch was 1.97±0.45 and the ultimate tensile engineering stress 2.1±0.2 MPa.

3.2 Relaxation tests

In the relaxation tests, the specimens were stretched 6 mm (35% failure displacement) and the displacement was maintained during 1,000 s. The normalized engineering stress-time curve of the experiments and its averaged response is illustrated in Figure 6b. The normalized engineering stress is the current stress divided by the peak stress. At the end of the 1,000s there was an 81±3.8% stress relaxation.

3.3 Fatigue tests

The fatigue tests consisted in 60 cycles of stretching the specimen until 10.3mm (60% failure displacement) and return the position until 7.7mm (45% failure displacement). The averaged response of the engineering stress-stretch curve and the engineering stress-time curve is illustrated in Figure 6c-d. Due to the amount of data in these graphics, we decided to present only the mean response. All the specimens presented visible permanent deformation after the fatigue tests, yet no macroscopic failure was visible.

The strain distribution in one example specimen, obtained from the digital image correlation, is illustrated in Figure 7. It shows the evolution of the strain field during the fatigue test. Each picture captures the specimen during a loading peak cycle, specifically during

the 1st, 20th, 40th and 60th peak cycle. The video with the strain distribution throughout the simulation is presented as supplementary material. The averaged measured permanent deformation was 7.37±2.20mm, which in terms of stretch corresponds to 1.49±0.15.

3.4 Histologic assessment

Figure 8 illustrates muscle-tendon sections from both control and tested specimens. All the pictures were obtained from the muscle portion approximately 5–15mm from the MTJ. Compared to the untested controls, it is possible to see significant fiber disruption and increase in the interstitial spaces in the specimens stretch at 60% failure displacement for 60 cycles. Figure 8f and g) illustrate individual fiber disruption occurring adjacent to apparently normal muscle fibers. Figure 8d and h) show kinked and distorted muscle fibers, which we take as one sign of cumulative damage.

Figure 9 shows sections from muscle-tendon specimens at the MTJ. Figure 9a-b show muscle fibers attaching to the collagen fibers from the tendon. Although the two sections are from tested specimens, both collagen and muscle fibers show a normal appearance. Figure 9c-d show an area of just collagen fibers, being d) a control specimen. Although collagen fibers seem to be more crimped in the untested specimen, there are no evident signs of damage in the collagen tissue.

Finally, Figure 10 shows structures from tendon-bone specimens. No signs of damage are visible in the muscle fibers (Figure 10a) in the collagen fibers (Figure 10c) or in the tendon-bone junction (Figure 10e).

3.5 Calibration of constitutive parameters

Using the micro-genetic algorithm, we calibrated the constitutive parameters to capture the visco-hyperelastic behavior, including the fatigue damage that we obtained from the experimental tests. Figure 11a and b compares the calibrated constitutive model from section 2.7 with the fatigue experimental data. We were more interested in capturing the stress decrease due to the viscoelastic behavior and due to the fatigue continuous damage, as such, we were more focused in capturing correctly the peak values in each loading cycle. Looking at all the data points in Figure 11a the coefficient of correlation is 0.891, not as good as when we focus only on the peak points (Figure 11b) which is 0.912. Moreover, the mean absolute error considering all the 3,212 data points was 0.051 MPa, while considering only the peak points it was 0.027 MPa. Since both absolute errors are lower than the precision of the stress calculation, which is 0.1 MPa (see section 2), we believe our correlation is sufficient to capture the behavior of the material. The calibrated material parameters are presented in Table 2.

3.6 Numerical analysis and interpretation of the specimen behavior

In this section we used the geometrical and material model described in section 2.7 to better interpret the experimental results from the fatigue tests and the overall mechanical behavior of the specimen. We performed a simulation of the fatigue tests using the complete constitutive model with the calibrated parameters described in Table 2, but also for a material that is only visco-hyperelastic, without damage, and one that is only hyperelastic

including damage. The purpose was to analyze separately the effects of viscoelasticity and the effects of material damage on the response of the biological materials.

Figure 11c shows the normalized engineering stress-time response for the three materials. The stress was normalized dividing by the peak value of each curve, which allows for a better comparison of the results. We can see that viscoelasticity is responsible for most of the energy dissipation in the first loading cycles. However, after approximately 10 loading cycles it reaches an almost equilibrium state, and the stress softening occurs mostly due to the continuous damage model. Combining both models, we have the solution that most approaches our experimental data. This confirms that our specimen has a characteristic behavior of a visco-hyperelastic material and that the 60 cycles at 60% failure displacement were sufficient to cause material damage.

4. Discussion

We believe that this is the first study investigating the biomechanical properties of the origin of the most caudal pelvic floor muscle, the ovine ishiococcygeous muscle, which serves as a homolog to the origin of the pubovisceral muscle in humans [6]. The primary finding of this research is that the origin of the ishiococcygeous muscle can accumulate low cycle fatigue damage under sub-maximal repetitive loading. This was observable not only in the stress-time curves but also in the microscopic analysis performed afterwards. The significance of the most caudal pelvic floor muscle is that in both the sheep and human, this muscle is the muscle that has to stretch the most in order to allow the fetal head to pass out of the birth canal, and it is the most likely to suffer a stretch-related injury.

As expected, the material behavior of the specimen was nonlinear and hyperelastic. This can be seen by the force-displacement curve from the ultimate tensile tests since the specimen was highly deformable and the relation between force and displacement was nonlinear (Figure 6a). We did not find data in the literature for the failure properties of the origin of the pubovisceral muscle in humans or animal models. However, there is *ex-vivo* data on human vaginal tissue, that has been reported to fail at a stress of 2.1–3.5 MPa and a stretch of 1.30–1.33 [15,36] and also on human pelvic ligaments, with the uterosacral ligament reportedly failing at a stress of 6.3 MPa and a stretch of 1.59 [37] and the round ligaments at a stress of 4.3 MPa and a stretch of 1.77 [37]. There is also one study that reports *ex-vivo* failure of a segment of human levator ani at a stress of approximately 0.24 MPa and a stretch of 1.37 [40]. Although these are different structures, it gives a baseline for the order of magnitude of the failure parameters of biological tissues in the pelvic region. We obtained a failure stress of 2.2 MPa and a failure stretch of 1.97, which is of the same order of magnitude of values found in the literature for tissues in the pelvic region providing some face validity.

The relaxation test allowed us to see that the origin of the ishiococcygeous muscle is highly viscoelastic since there is a significant stress relaxation when maintaining the same displacement for 1000 s. In fact, we obtained an 81% decrease of the stresses after the 1000 s (Figure 6b). Viscoelasticity is extremely important for biological tissues, but most especially for tissues in the female pelvis, since it allows tissues to withstand larger deformations with less damage [1]. This is particularly important during childbirth since it

is the relaxation of the vagina and other pelvic floor tissues over time that allow further dilatation as labor progresses [24].

The mechanical effect captured from the fatigue tests confirms both the nonlinear hyperelastic and viscoelastic behavior. During the first cycle there is a significant hysteresis, which indicates a substantial energy dissipation. Over time the effects of hysteresis diminish, but not to an equilibrium state. This equilibrium state means that over time a steady state would be reached in the response of the tissue, typically in 10–20 cycles, if there was no damage to the material [1,38]. However, it can be seen in the stress-stretch curve and in the stress-time curve that our material does not reach a steady state in the 60 cycles (Figure 6c and d). This indicates that there is continuous energy dissipation for which material damage is responsible. Besides the indication of damage due to the energy dissipation seen in the stretch-time curves, we also observed macroscopically that the specimen exhibited permanent deformation after the fatigue tests. However, no macroscopic tears were visible during and after the test. So what might be responsible?

The histological analysis took our findings to another level. It confirmed the presence of damage at the microscopic scale and showed the weakest regions of the bone-tendon-muscle unit that constitutes the origin of the ishiococcygeous muscle. The main findings were individual muscle fiber rupture and kinked muscle fibers that occurred in the muscle in an approximately 5–15 mm region of the MTJ (Figure 9). Importantly, neither the MTJ nor the tendon-bone sections showed any apparent sign of damage (Figure 10). Moreover, we could not identify obvious signs of damage in the collagen fibers, although compared with the untested controls, fatigued specimens did seem to have less crimped collagen fibers (Figure 9c and d, Figure 10c and d). This is consistent with the results from the strain distribution obtained through the speckle pattern (Figure 7) that shows engineering strains of approximately 0.85 in the muscle and musculotendinous region, but only 0.15–0.45 in the tendon and tendon-bone region for the same globally applied stretch. So, we rejected our working hypothesis and instead accepted one of the alternatives hypotheses, namely that the accumulation of damage occurred at a different site than the tendon-bone junction. In particular, we verified accumulation of damage in the muscle fibers near the MTJ.

To have a better understanding of the characteristic behavior of our specimen, we developed and implemented a visco-hyperelastic material model including continuous damage. Using the finite element software ABAQUS® and the user-defined subroutine UMAT, we were able to simulate the fatigue test mimicking our experimental protocol. We included the material having a visco-hyperelastic behavior because of the experimental fatigue curves that we obtained. We were able to confirm that behavior by performing the same simulation considering only an hyperelastic material with continuous damage and a visco-hyperelastic material without damage. We saw that the viscoelasticity is responsible for the major energy loss in the first 3–4 cycles (Figure 11c). This is a defense mechanism of soft biological tissues, since for the same applied stretch, the stresses decrease, allowing tissues to withstand larger deformations with less damage. On the other hand, the continuous stress softening that is observed throughout the remaining loading cycles does not occur due to viscoelasticity. Comparing the purely visco-hyperelastic material with the visco-hyperelastic material including continuous damage, we can see that after 3–4 cycles the

stresses continue to significantly decrease for the material where damage is considered. For the visco-hyperelastic material without damage, there are only minor decreases, because the material reaches an equilibrium. However, this stress softening that is associated with continuous damage is not a defense mechanism as it occurs with viscoelasticity. On the contrary, it occurs because the repetitive loading causes material damage accumulation capable of affecting the microscopic-scale mechanical properties of the material. In other words, it weakens the material, making it more prone to tear due to a load that in an undamaged state would not be enough to cause failure.

Numerous studies have been focused on the effects of cyclic loading in collagen fibers and collagen fibrils, reporting signs of accumulated damage as kinked patterns in the collagen fibers and fiber disruption [5,16,46,51,52]. According to Fung, D.T *et al.* [16], initial fatigue loading lengthens the collagen fibers from a crimped to an uncrimped state. Continued loading causes stretching of a local population of collagen fibers into their plastic range of deformation, causing the formation of kinked deformation patterns. Further loading leads to rupture of the plastically deformed collagen fibers. However, only the tendon or other collagenous structures were being tested in those studies. Here, we included the complete muscle origin and show that the weakest region in the passive ishiococcygeous muscle is the muscle near the MTJ. The collagen fibers showed significant less deformation and after the 60 loading cycles they only appear to be less crimped than the untested controls. This is consistent with the initial fatigue loading phase postulated by Fung, D.T *et al.* [16]. One interesting fact is that cyclic loading seems to affect the muscle fibers in a similar way than the collagen fibers, since we could see in the histological analysis that the muscle fibers are deformed into their plastic range, which caused kinked muscle fibers and fiber disruption.

The present study has several limitations. First, our specimens came from non-pregnant sheep and since it is expected that pregnant pelvic tissues are more compliant [43], the amount of damage may have been overestimated in this study if one is considering the second stage of labor. Secondly, this was an *in vitro* study of passive inert muscle and the muscle-tendon-bone unit may behave differently *in vivo*, especially given that active contractions can occur. With active contractions the muscle and collagen fiber stress would be expected to increase [7], so considering this aspect, our present observations of the extent of damage accumulation may be conservative. Thirdly, we froze the specimens once, which might have had some influence on the tissues [19], although we bore that in mind when studying the histological sections. Fourthly, we saw with the speckle pattern that the strain distribution is not the same throughout the specimen, so interpretation of the engineering stress-strain curves needs to take that into account. In effect, they represent an averaged overall behavior of the bone-tendon-muscle unit. Fifthly, the digital image correlation software did not work over the duration of the experiment for all the specimens, so we did not obtain the strain field throughout the fatigue experiment in the 13 tested specimens. We believe this happened since we have a high deformation and a long experiment, which caused the software to lose correlation of the speckle points as the experiment progressed in some of the specimens. In the future we plan to test beforehand better ways to apply the speckle pattern in order to overcome this problem. Lastly, from a structural point of view the part of the ishciococcygeal muscle that is the closest homolog to the human pubovisceral muscle is the part that inserts onto the sheep lateral vagina, in a similar manner that the pubovisceral

muscle inserts onto the human perineal body and lateral vagina. Hence it might be fruitful in the future to focus on the mechanical behavior of this subdivision of the muscle (i.e., the medial- most of the two 'TM' specimens visible on the right side of Figure 4).

Nevertheless, we believe this study is the first to characterize biomechanically the origin of the ishiococcygeous muscle, a homologous structure to the origin of the pubovisceral muscle in humans. It showed that the complete bone-tendon-muscle origin exhibits a nonlinear and highly viscoelastic behavior, even in a non-pregnant state. The weakest region is the muscle near the MTJ, which is the material that has the highest deformation for the same applied stretch. When cyclically stretched at a sub-maximal displacement, it is capable of accumulating damage at a microscopic level, which weakens the material. The evidence of damage accumulation included kinked muscle fibers and muscle fiber disruption in the areas with higher deformation, namely in the muscle near the MTJ. We also developed a material constitutive model, applicable in ABAQUS® finite element software, that was able to capture the stress softening due to viscoelasticity and the continuous damage. This can be useful for testing more complex loading scenarios that occur during the second stage of labor.

We believe that this work can guide future studies on the origin of the pubovisceral muscle. Future work should be focused on verifying our findings in pregnant tissues and in human specimens, if possible. This is an important topic since the origin of the pubovisceral muscle is commonly torn, sometimes completely so, during a difficult vaginal delivery; it is never repaired because the surgical risk outweighs any benefit. Understanding the behavior of the weakest region of the bone-tendon-muscle unit is important in helping to improve the management of injury afterwards. But even more important is the urgent need to prevent the injury in the first place. If our results are corroborated by others, understanding that the muscle can accumulate damage with repetitive large loading cycles, which can weaken the region and make it prone to tear, could lead to a change and standardization in the management of labor. Currently, there are different pushing techniques that lead to different pushing patterns that cause different numbers of pubovisceral muscle loading cycles during the second stage of labor [31].

This is the first study to show the possibility of fatigue damage accumulating at the origin of the last pelvic floor muscle engaged by the fetal head during delivery, namely the ishiococcygeous muscle in sheep, which corresponds to the pubovisceral muscle in humans, the muscle that undergoes the greatest stretch at the end of the second stage of delivery. Although further studies are needed, we hope that our findings trigger additional research in this area that can ultimately lead to designing an improved management of labor, with better outcomes for the mother.

5. Conclusions

Our findings showed that the origin of the ishiococcygeous muscle from mature sheep, a muscle that is homologous to the pubovisceral muscle in humans, can accumulate damage at the microscopic level due to a sub-maximal repetitive loading of only 60 cycles at 60% failure displacement. This damage accumulation was seen in the muscle from 5 to

15 mm from the MTJ. Evidence of damage was the presence of kinked muscle fibers, indicating permanent deformation, and individual muscle fiber rupture. Although there was not sufficient data to confirm this, it is possible that the first stage of fatigue is the permanent deformation of muscle fibers, which cause the fiber kinking. With the continuity of the loading cycles those kinked fibers eventually tear. Besides the microscopic evidence of damage, the 60 cycles at 60% failure displacement were sufficient to affect the mechanical properties of the specimen, as seen by the continued energy dissipation in the stress-time curve.

This work showed that the weakest region in the bone-tendon-muscle unit of the ovine ishiococcygeous muscle origin to be the muscle near the MTJ, and that muscle can accumulate damage due to a repetitive sub-maximal loading that negatively affects its mechanical properties.

Supplementary Material

Refer to Web version on PubMed Central for supplementary material.

Acknowledgements

Research reported in this publication was supported by U.S. Public Health Service awards P30 AG024824 and P30 AR069620. The content is solely the responsibility of the authors and does not represent the official views of the U.S. National Institutes of Health. Authors also acknowledge the support from the Portuguese Foundation for Science and Technology (FCT) under grant SFRH/BD/136213/2018 and under the research project UIDB/50022/2020.

The authors thank the University of Michigan Department of Orthopedic Surgery Histology Core and Carol Whitinger for training the first author in the paraffin embedder, microtome and tissue staining and also for performing the initial paraffin processing and bone decalcification of our samples. We thank Professor Susan V. Brooks for teaching us how to interpret the histological images of muscle and tendon. We also thank the University of Michigan Soft Tissues Research Lab, directed by Professor Ellen M. Arruda, for making available the tensile test machine and the digital image correlation equipment and Andrea Poli for helping with the design and performance of the experimental tests. For providing the specimens used in this work, we thank the Meat Laboratory of the Michigan State University and the Experimental Surgical Services from the University of Minnesota. Finally, we thank Professor John O.L. DeLancey for consultations and help with the first sheep pelvis dissection.

References

1. Abramowitch S, Easley D. Chapter Four - Introduction to Classical Mechanics. In: Hoyte L, Damaser MBT-B of the FPF, eds. Academic Press; 2016:89–107. doi:10.1016/B978-0-12-803228-2.00004-0
2. Abramowitch SD, Feola A, Jallah Z, Moalli PA. Tissue mechanics, animal models, and pelvic organ prolapse: A review. Eur J Obstet Gynecol Reprod Biol 2009;144:S146–S158. doi:10.1016/j.ejogrb.2009.02.022 [PubMed: 19285776]
3. Alshomer F, Chaves C, Kalaskar DM. Advances in Tendon and Ligament Tissue Engineering: Materials Perspective. Bandyopadhyay A, ed. J Mater 2018;2018. doi:10.1155/2018/9868151
4. Ashton-Miller JA, DeLancey JOL. Functional anatomy of the female pelvic floor. Ann N Y Acad Sci 2007;1101:266–296. doi:10.1196/annals.1389.034 [PubMed: 17416924]
5. Baldwin SJ, Kreplak L, Lee JM. Characterization via atomic force microscopy of discrete plasticity in collagen fibrils from mechanically overloaded tendons: Nano-scale structural changes mimic rope failure. J Mech Behav Biomed Mater 2016;60:356–366. doi:10.1016/j.jmbbm.2016.02.004 [PubMed: 26925699]
6. Bassett EG. The anatomy of the pelvic and perineal regions of the ewe. Aust J Zool 1965;13(2):201–242.

7. Brooks SV, Zerba E, Faulkner JA. Injury to muscle fibres after single stretches of passive and maximally stimulated muscles in mice. J Physiol 1995;488(2):459–469. doi:10.1113/jphysiol.1995.sp020980 [PubMed: 8568684]
8. Budday S, Sommer G, Birkl C, et al. Mechanical characterization of human brain tissue. Acta Biomater 2017;48:319–340. doi:10.1016/j.actbio.2016.10.036 [PubMed: 27989920]
9. Chen J, Kim J, Shao W, et al. An anterior cruciate ligament failure mechanism. Am J Sports Med 2019;47(9):2067–2076. doi:10.1177/0363546519854450 [PubMed: 31307223]
10. Cheng S, Clarke EC, Bilston LE. The effects of preconditioning strain on measured tissue properties. J Biomech 2009;42(9):1360–1362. doi:10.1016/j.jbiomech.2009.03.023 [PubMed: 19394022]
11. Couri BM, Lenis AT, Borazjani A, Paraiso MFR, Damaser MS. Animal models of female pelvic organ prolapse: lessons learned. Expert Rev Obstet Gynecol 2012;7(3):249–260. doi:10.1586/eog.12.24 [PubMed: 22707980]
12. DeLancey JOL, Kearney R, Chou Q, Speights S, Binno S. The appearance of levator ani muscle abnormalities in magnetic resonance images after vaginal delivery. Obstet Gynecol 2003;101(1):46–53. doi:10.1016/S0029-7844(02)02465-1 [PubMed: 12517644]
13. DeLancey JOL, Sørensen HC, Lewicky-Gaupp C, Smith TM. Comparison of the puborectal muscle on MRI in women with POP and levator ani defects with those with normal support and no defect. Int Urogynecol J 2012;23(1):73–77. doi:10.1007/s0019-2011-1527-8 [PubMed: 21822711]
14. Dietz HP, Gillespie AVL, Phadke P. Avulsion of the pubovisceral muscle associated with large vaginal tear after normal vaginal delivery at term. Aust New Zeal J Obstet Gynaecol 2007;47(4):341–344. doi:10.1111/j.1479-828X.2007.00748.x
15. Ferreira JPS, Rynkevic R, Martins PALS, et al. Predicting the mechanical response of the vaginal wall in ball burst tests based on histology. J Biomed Mater Res Part B Appl Biomater 2019;n/a(n/a). doi:10.1002/jbm.b.34534
16. Fung DT, Wang VM, Laudier DM, et al. Subrupture tendon fatigue damage. J Orthop Res 2009;27(2):264–273. doi:10.1002/jor.20722 [PubMed: 18683881]
17. Gao Y, Zhao Z, Yang Y, Zhang M, Wu J, Miao Y. Diagnostic value of pelvic floor ultrasonography for diagnosis of pelvic organ prolapse: a systematic review. Int Urogynecol J 2020;31(1):15–33. doi:10.1007/s00192-019-04066-w [PubMed: 31485686]
18. Ghetti C, Skoczylas LC, Oliphant SS, Nikolajski C, Lowder JL. The Emotional Burden of Pelvic Organ Prolapse in Women Seeking Treatment: A Qualitative Study. Female Pelvic Med Reconstr Surg 2015;21(6):332–338. doi:10.1097/SPV.0000000000000190 [PubMed: 26506161]
19. Gottsauner-Wolf F, Grabowski JJ, Chao EY, An KN. Effects of freeze/thaw conditioning on the tensile properties and failure mode of bone-muscle-bone units: a biomechanical and histological study in dogs. J Orthop Res 1995;13(1):90–95. doi:10.1002/jor.1100130114 [PubMed: 7853109]
20. Holzapfel GA. Nonlinear Solid Mechanics: A Continuum Approach for Engineering John Wiley & Sons; 2000.
21. Holzapfel GA, Gasser TC. A viscoelastic model for fiber-reinforced composites at finite strains: Continuum basis, computational aspects and applications. Comput Methods Appl Mech Eng 2001;190(34):4379–4403. doi:10.1016/S0045-7825(00)00323-6
22. Holzapfel GA, Gasser TC, Ogden RW. A new constitutive framework for arterial wall mechanics and a comparative study of material models. J Elast Phys Sci solids 2000;61(1):1–48. doi:10.1023/A:1010835316564
23. Hoyte L, Damaser MS, Warfield SK, et al. Quantity and distribution of levator ani stretch during simulated vaginal childbirth. Am J Obstet Gynecol 2008;199(2):198.e1–5. doi:10.1016/j.ajog.2008.04.027 [PubMed: 18513684]
24. Jing D, Ashton-Miller JA, DeLancey JOL. A subject-specific anisotropic visco-hyperelastic finite element model of female pelvic floor stress and strain during the second stage of labor. J Biomech 2012;45(3):455–460. doi:10.1016/j.jbiomech.2011.12.002 [PubMed: 22209507]
25. Kearney R, Sawhney R, DeLancey JOL. Levator ani muscle anatomy evaluated by origin-insertion pairs. Obstet Gynecol 2004;104(1):168–173. doi:10.1097/01.AOG.0000128906.61529.6b [PubMed: 15229017]

26. Kim J, Betschart C, Ramanah R, Ashton-Miller JA, DeLancey JOL. Anatomy of the pubovisceral muscle origin: Macroscopic and microscopic findings within the injury zone. Neurourol Urodyn 2015;34(8):774–780. doi:10.1002/nau.22649 [PubMed: 25156808]
27. Kim J, Ramanah R, DeLancey JOL, Ashton-Miller JA. On the anatomy and histology of the pubovisceral muscle enthesis in women. Neurourol Urodyn 2011;30(7):1366–1370. doi:10.1002/nau.21032 [PubMed: 21567449]
28. Koyucu RG, Demirci N. Effects of pushing techniques during the second stage of labor: A randomized controlled trial. Taiwan J Obstet Gynecol 2017;56(5):606–612. doi:10.1016/j.tjog.2017.02.005 [PubMed: 29037544]
29. Laganà AS, La Rosa VL, Rapisarda AMC, Vitale SG. Pelvic organ prolapse: the impact on quality of life and psychological well-being. J Psychosom Obstet Gynecol 2018;39(2):164–166. doi:10.1080/0167482X.2017.1294155
30. de Leeuw JW, Struijk PC, Vierhout ME, Wallenburg HC. Risk factors for third degree perineal ruptures during delivery. BJOG 2001;108(4):383–387. [PubMed: 11305545]
31. Lien K-C, DeLancey JOL, Ashton-Miller JA. Biomechanical analyses of the efficacy of patterns of maternal effort on second-stage progress. Obstet Gynecol 2009;113(4):873–880. doi:10.1097/AOG.0b013e31819c82e1 [PubMed: 19305333]
32. Lien K-C, Mooney B, DeLancey JOL, Ashton-Miller JA. Levator ani muscle stretch induced by simulated vaginal birth. Obstet Gynecol 2004;103(1):31–40. doi:10.1097/01.AOG.0000109207.22354.65 [PubMed: 14704241]
33. Lipps DB, Wojtys EM, Ashton-Miller JA. Anterior cruciate ligament fatigue failures in knees subjected to repeated simulated pivot landings. Am J Sports Med 2013;41(5):1058–1066. doi:10.1177/0363546513477836 [PubMed: 23460331]
34. Margulies RU, Huebner M, DeLancey JOL. Origin and insertion points involved in levator ani muscle defects. Am J Obstet Gynecol 2007;196(3):251.e1–251.e5. doi:10.1016/j.ajog.2006.10.894 [PubMed: 17346542]
35. Marino M. Constitutive modeling of soft tissues. In: Narayan R, ed. Encyclopedia of Biomedical Engineering Vol 1–3. Elsevier; 2019:81–110. doi:10.1016/B978-0-12-801238-3.99926-4
36. Martins P, Lopes Silva-Filho A, Rodrigues Maciel da Fonseca AM, et al. Biomechanical properties of vaginal tissue in women with pelvic organ prolapse. Gynecol Obstet Invest 2013;75(2):85–92. doi:10.1159/000343230 [PubMed: 23295833]
37. Martins P, Silva-Filho AL, Fonseca AMRM, et al. Strength of round and uterosacral ligaments: a biomechanical study. Arch Gynecol Obstet 2013;287(2):313–318. doi:10.1007/s00404-012-2564-3 [PubMed: 23001414]
38. Meyers MA, Chawla KK. Mechanical Behaviour of Materials Cambridge University Press; 2009.
39. Milella PP. Fatigue and Corrosion in Metals 1st ed. (Milella PP, ed.). Springer-Verlag Mailand; 2013. doi:10.1007/978-88-470-2336-9
40. Nagle AS, Barker MA, Kleeman SD, Haridas B, Mast TD. Passive biomechanical properties of human cadaveric levator ani muscle at low strains. J Biomech 2014;47(2):583–586. doi:10.1016/j.jbiomech.2013.11.033 [PubMed: 24342498]
41. Parente MPL, Jorge RMN, Mascarenhas T, Fernandes AA, Martins JAC. Deformation of the pelvic floor muscles during a vaginal delivery. Int Urogynecol J Pelvic Floor Dysfunct 2008;19(1):65–71. doi:10.1007/s00192-007-0388-7 [PubMed: 17522755]
42. Peña E. Computational aspects of the numerical modelling of softening, damage and permanent set in soft biological tissues. Comput Struct 2014;130:57–72. doi:10.1016/j.compstruc.2013.10.002
43. Rynkevic R, Martins P, Hympanova L, Almeida H, Fernandes AA, Deprest J. Biomechanical and morphological properties of the multiparous ovine vagina and effect of subsequent pregnancy. J Biomech 2017;57:94–102. doi:10.1016/j.jbiomech.2017.03.023 [PubMed: 28454911]
44. Samadi-Dooki A, Voyiadjis GZ. A fully nonlinear viscohyperelastic model for the brain tissue applicable to dynamic rates. J Biomech 2019;84:211–217. doi:10.1016/j.jbiomech.2019.01.007 [PubMed: 30678890]
45. Samuelsson E, Ladfors L, Lindblom BG, Hagberg H. A prospective observational study on tears during vaginal delivery: occurrences and risk factors. Acta Obstet Gynecol Scand 2002;81(1):44–49. [PubMed: 11942886]

46. Silver FH, Jaffe M, Shah RG. 11 - Structure and behavior of collagen fibers. In: Bunsell ARBT-H of P of T and TF (Second E, ed. The Textile Institute Book Series Woodhead Publishing; 2018:345–365. doi:10.1016/B978-0-08-101272-7.00011-0
47. Tadros AS, Huang BK, Pathria MN. Muscle-Tendon-Enthesis Unit. Semin Musculoskelet Radiol 2018;22(03):263–274. doi:10.1055/s-0038-1641570 [PubMed: 29791955]
48. Torp SB, Friedman B. Effects of Age and of mechanical deformation on the ultrastructure of tendon. In: Proceedings of the Colston Conference. University of Bristol; 1974:223–250.
49. Urbankova I, Vdoviakova K, Rynkevic R, et al. Comparative Anatomy of the Ovine and Female Pelvis. Gynecol Obstet Invest 2017;82(6):582–591. doi:10.1159/000454771 [PubMed: 28125816]
50. VanDusen K, Larkin L. Muscle-tendon interface. In: Regenerative Engineering of Musculoskeletal Tissues and Interfaces ; 2015:409–429. doi:10.1016/B978-1-78242-301-0.00017-3
51. Veres SP, Harrison JM, Lee JM. Repeated subrupture overload causes progression of nanoscaled discrete plasticity damage in tendon collagen fibrils. J Orthop Res 2012;31(5):731–737. doi:10.1002/jor.22292 [PubMed: 23255142]
52. Veres SP, Lee JM. Designed to fail: A novel mode of collagen fibril disruption and its relevance to tissue toughness. Biophys J 2012;102(12):2876–2884. doi:10.1016/j.bpj.2012.05.022 [PubMed: 22735538]
53. Wilkins MF, Wu JM. Lifetime risk of surgery for stress urinary incontinence or pelvic organ prolapse. Minerva Ginecol 2017;69(2):171–177. doi:10.23736/S0026-4784.16.04011-9 [PubMed: 28001022]
54. Woo SL, Fisher MB, Feola AJ. Contribution of Biomechanics to Management of Ligament and Tendon Injuries. Mol cell Biomech 2008;5(1):49–68. [PubMed: 18524246]
55. Zielinski R, Miller J, Low LK, Sampselle C, Delancey JOL. The relationship between pelvic organ prolapse, genital body image, and sexual health. Neurourol Urodyn 2012;31(7):1145–1148. doi:10.1002/nau.22205 [PubMed: 22473490]
56. Zuskov A, Freedman BR, Gordon JA, Sarver JJ, Buckley MR, Soslowsky LJ. Tendon Biomechanics and Crimp Properties Following Fatigue Loading Are Influenced by Tendon Type and Age in Mice. J Orthop Res 2020;38(1):36–42. doi:10.1002/jor.24407 [PubMed: 31286548]

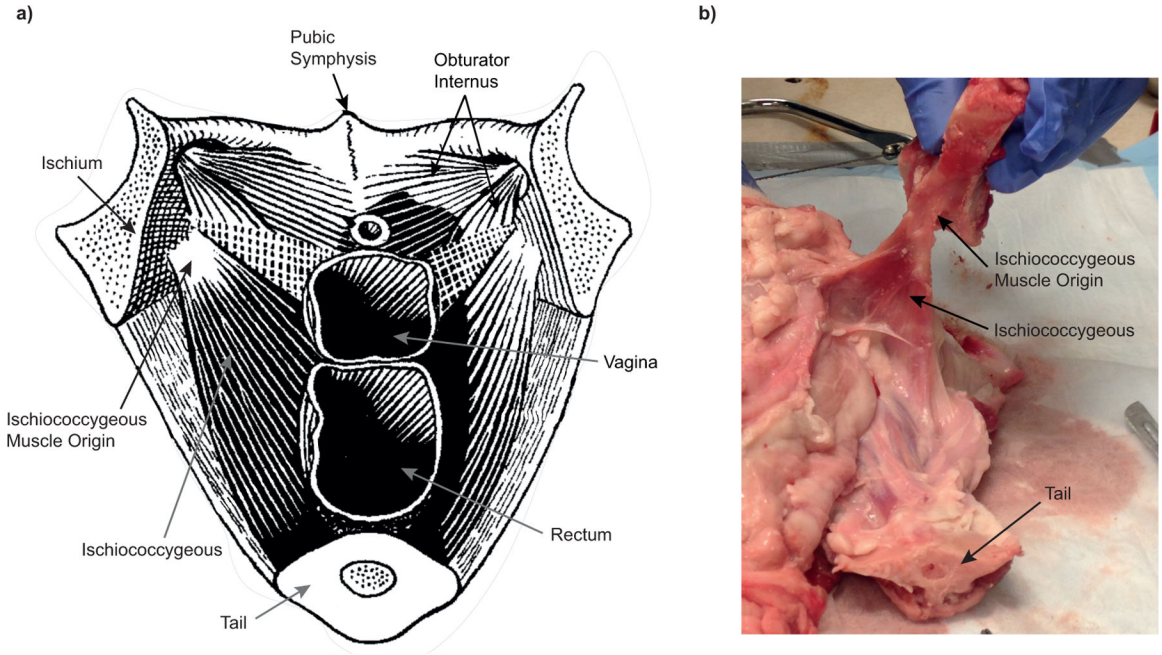

Figure 1 -

Superior view of the ovine pelvic floor. **a)** schematic representation showing the origin and insertion of the ishiococcygeous muscle, adapted from Basset. E.G [6]. **b)** posterolateral image showing the origin of the left ishiococcygeous muscle (pubic bone already trimmed at the proximal end) and the muscle fanning out and inserting onto to vaginal wall, anal canal, and coccygeal bone of tail.

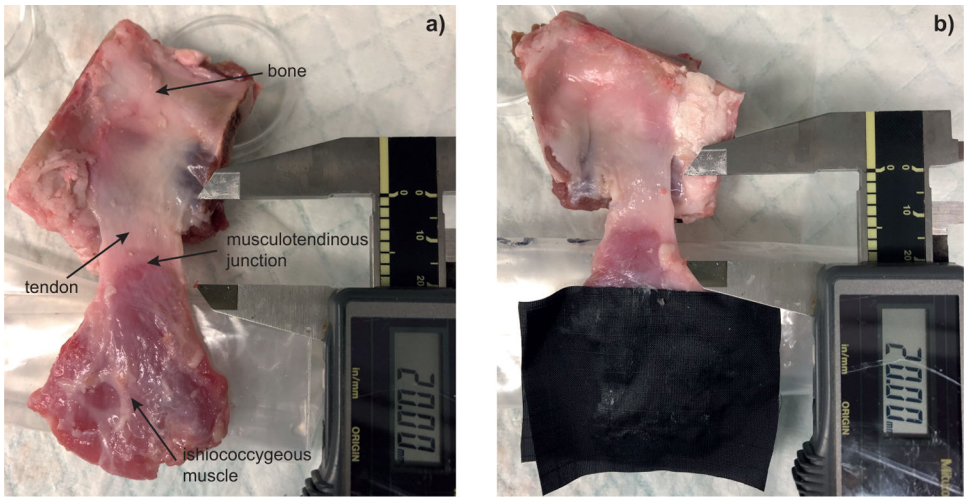

Figure 2 -

An anterolateral view of the ischiococcygeus muscle specimen after dissection: **a)** prior to preparation the medial surface of the (left) pubic bone can be seen at top with the bony origin (white collagenous tissue) of the muscle visible to the left of the small rectangular-shaped piece of clear skin tape (which itself lies over where the obturator foramen would normally be, the ischiococcygeus tendon with undisturbed margins, the MTJ and muscle proper below; **b)** after preparation consisting of adhering the ripstop nylon to both side of the muscle to within 15 mm of the MTJ. The jaws of the digital caliper serve as a 20 mm scale.

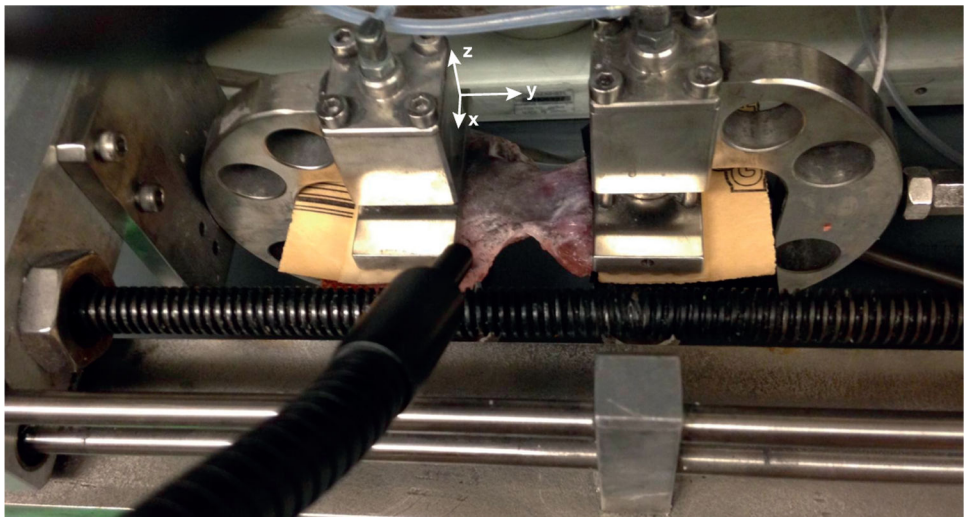

Figure 3 -
Specimen inserted in the setup, hydrated with PBS, and ready for testing.

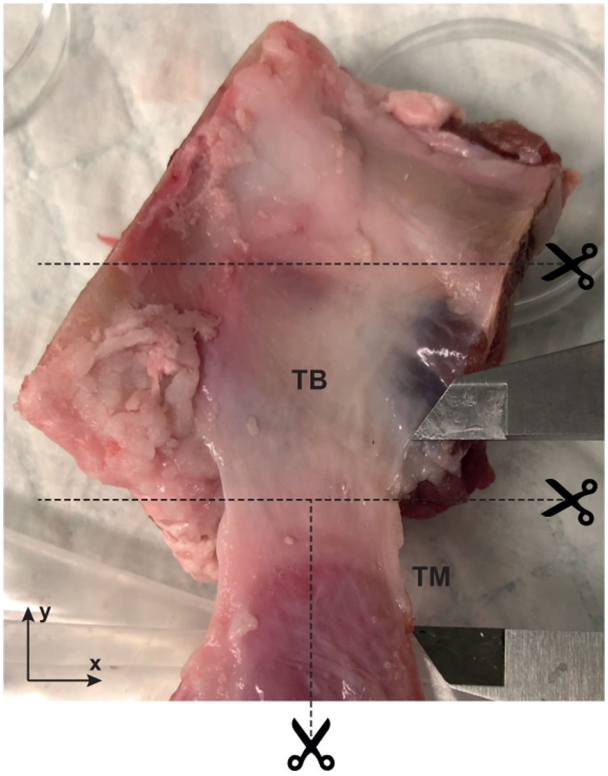

Figure 4 -

Illustration showing how ischiococcygeal muscle specimens were divided (dashed lines with scissor logo) for histological evaluation: Tendon-Bone (TB) and Tendon-Muscle (TM) sections. Tendon-Bone samples were sliced with the microtome in the y-z plane. Tendon-Muscle samples were divided in two, according to the figure, and one section was sliced in the y-x plane while the second was sliced in the y-z plane.

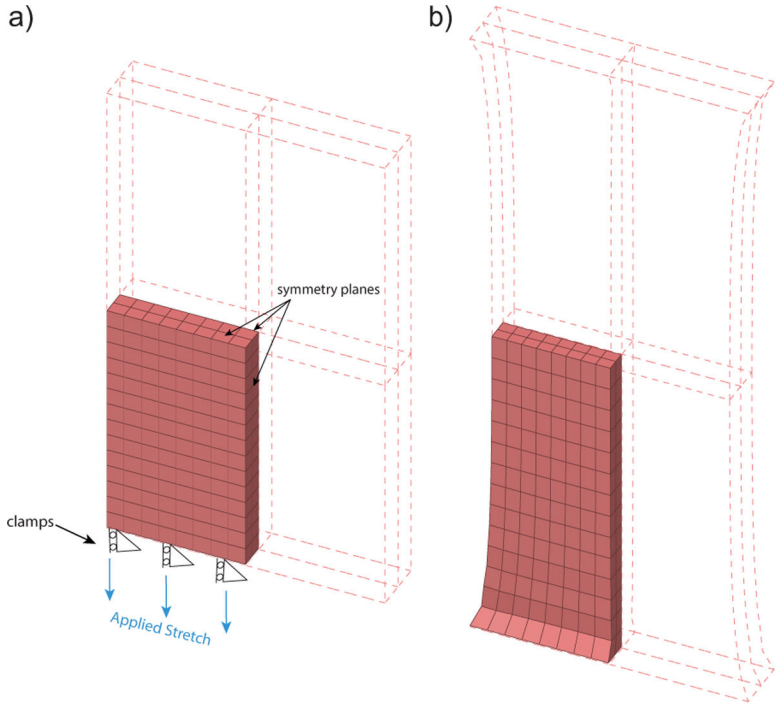

Figure 5 -

Finite Element model for the simulation of the experimental fatigue tests integrated in the micro-genetic algorithm for the calibration of the constitutive model parameters. The finite element model consists in a simplification of 1/8 of the averaged specimen. Representation of the boundary conditions and direction of the applied stretch. **a)** initial configuration **b)** deformed configuration at the peak displacement.

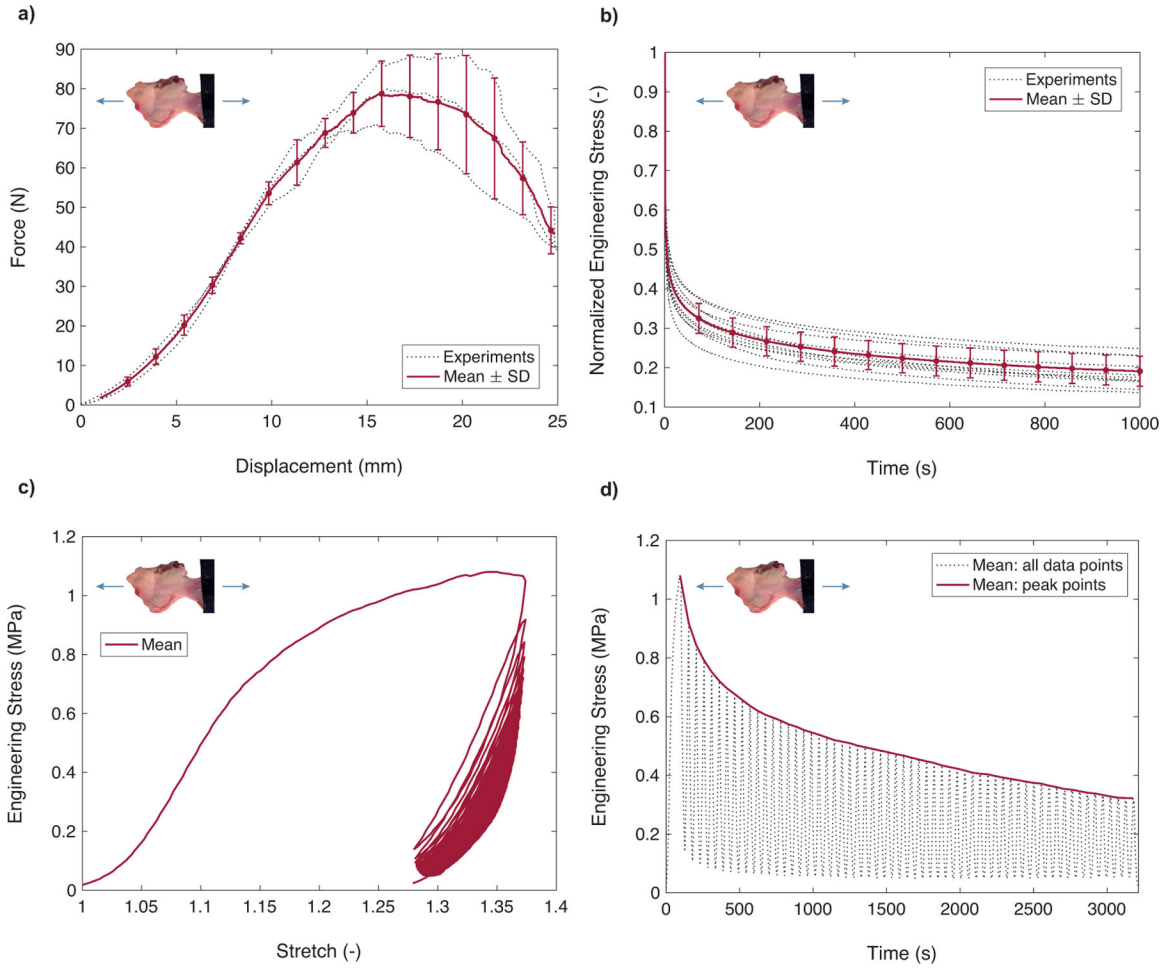

Figure 6 -

Force-displacement curves from the ultimate tensile tests (dashed lines). **a)** Averaged response: mean ± SD (standard deviation) (solid line). **b)** Averaged response of the relaxation tests: normalized engineering stress (current stress/peak stress) of all the experiments (dashed lines). Averaged response: mean ± SD (solid line). **c-d)** Averaged response of the fatigue tests **c)** engineering stress-grip to grip stretch **d)** engineering stress-time.

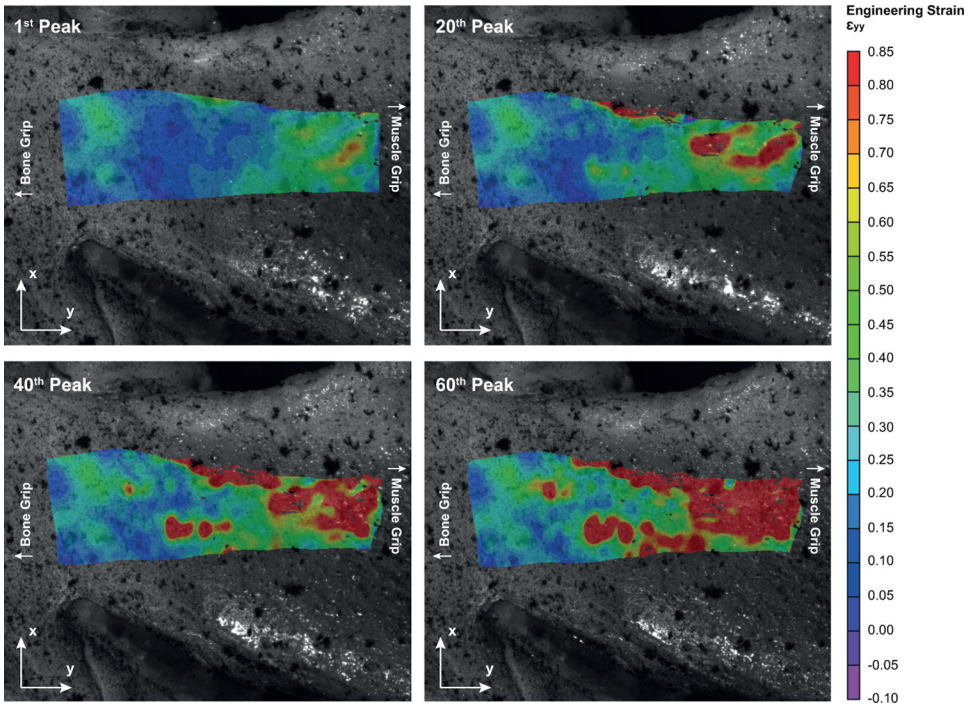

Figure 7 -

Evolution of the engineering strain εyy distribution throughout the fatigue test in specimen 6R.

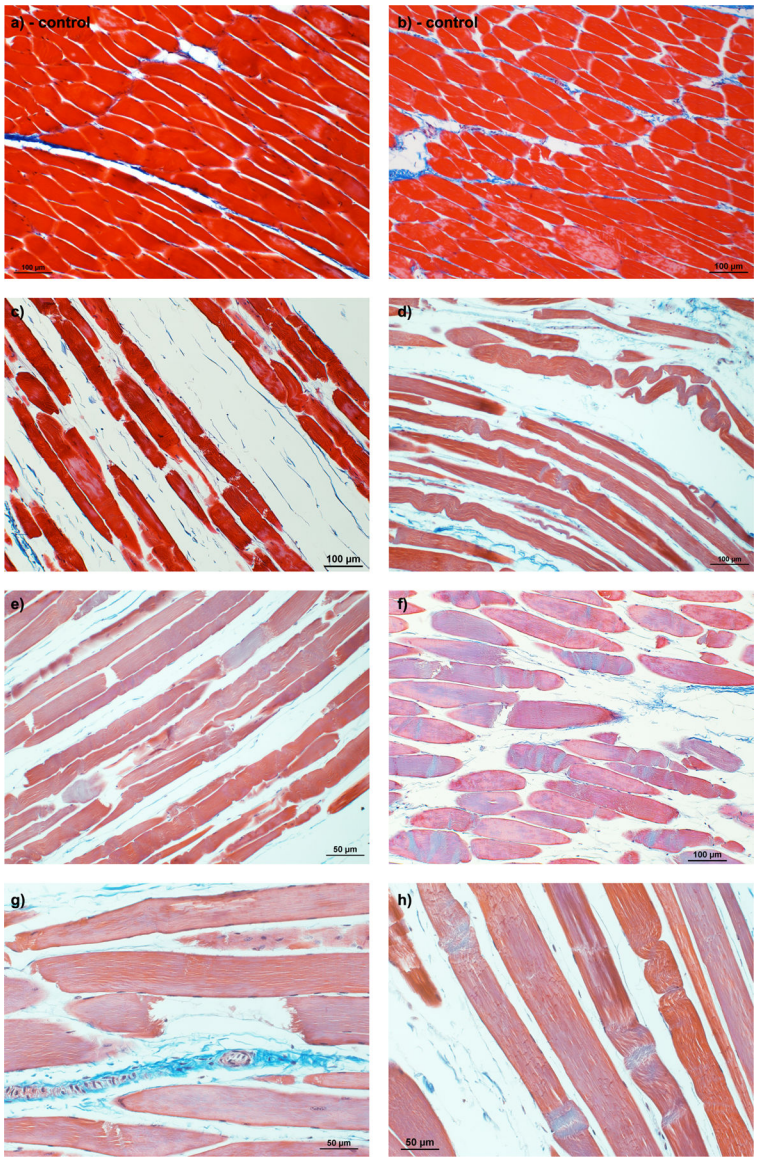

Figure 8 -

Histological appearance of muscle-tendon sections with Masson's Trichrome stain. Comparison between untested controls **(a-b)** and fatigued specimens **(c-h)** (60 cycles between 60% and 45% of failure displacement). Fatigued specimens show kinked muscle fibers, individual fibers disruption and increase in interstitial spaces. **a)** Specimen 4L – control (~5–10mm of MTJ, ×10) **b)** Specimen 4L – control (~10–15mm of MTJ, ×10) **c)** Specimen 5R (~10–15mm of MTJ, ×10) **d)** Specimen 10L (~10–15mm of MTJ, × 10) **e)** Specimen 10R (~10–15mm of MTJ, ×10). **f)** Specimen 5L (~10–15mm of MTJ, ×10) **g)** Specimen 10L (~10–15mm of MTJ, ×20) **h)** Specimen 10L (~5–10mm of MTJ, ×20).

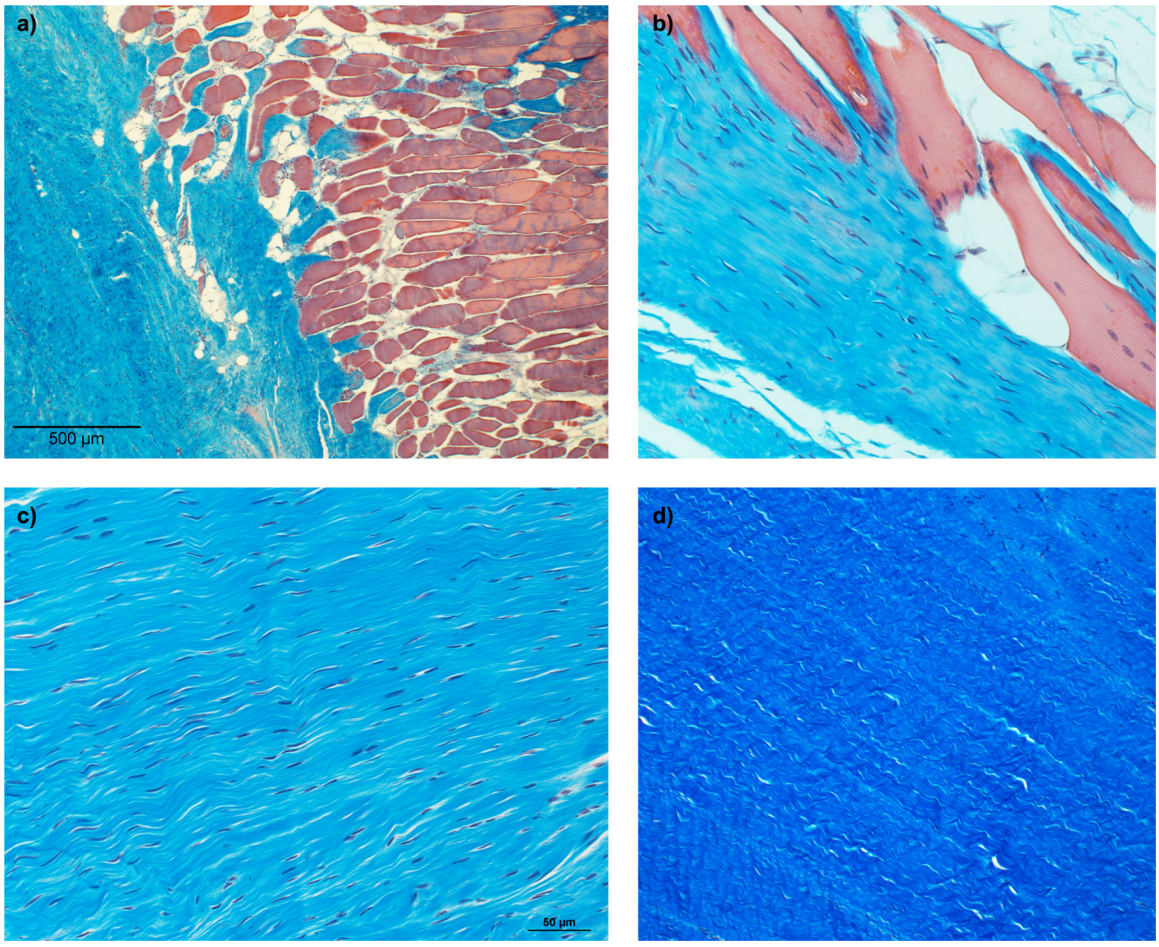

Figure 9 -

Histological appearance of muscle-tendon sections at the MTJ with Masson's Trichrome stain. Collagen and muscle fibers with normal appearance in the MTJ and in the collagen fibers. **a)** Specimen 9L (×4). **b)** Specimen 10L (×20). **c)** Specimen 10R (×20). **d)** Specimen 4L – control (×10).

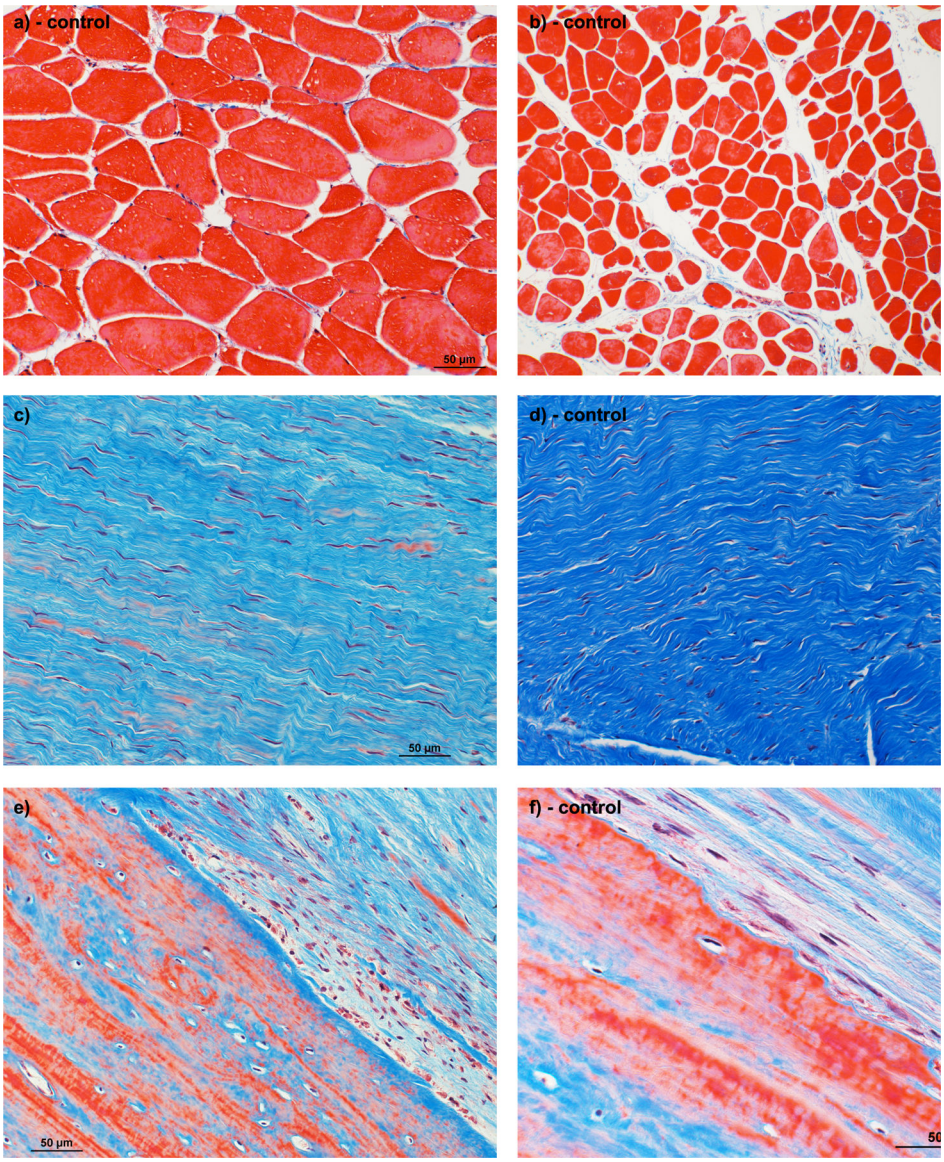

Figure 10 -

Histological appearance of tendon-bone sections with Masson's Trichrome stain with normal appearance comparing untested controls and fatigued specimens (60 cycles between 60% and 45% of failure displacement) shows a normal appearance. **a)** Specimen 5L (×20) **b)** Specimen 3R- control (×10) **c)** Specimen 5R (×20) **d)** Specimen 4L – control (×20) **e)** Specimen 5R (×20) **f)** Specimen 3R – control (×40).

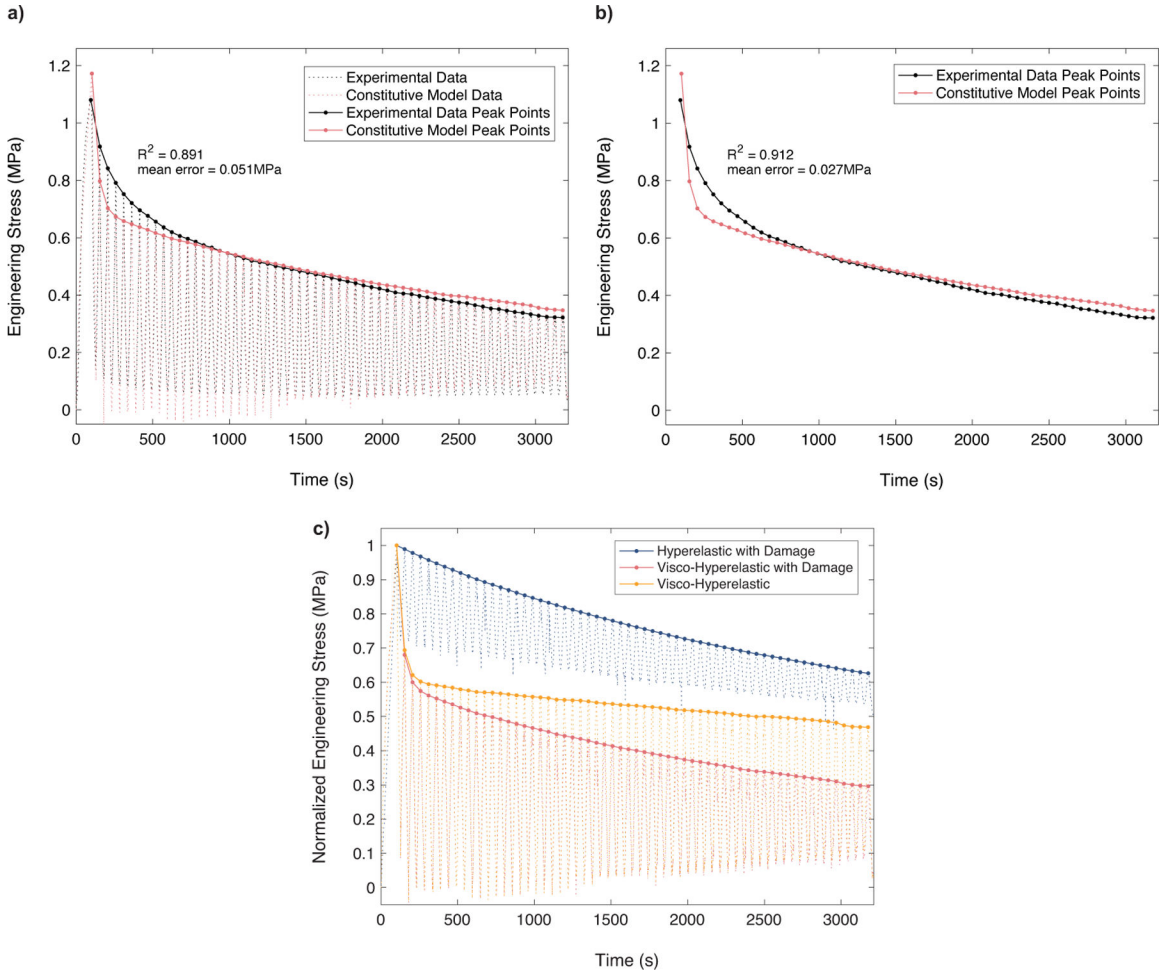

Figure 11 -

a-b) Calibration of constitutive model parameters for the averaged response of the fatigue tests. **a)** comparison and coefficient of correlation with all the 3212 data points. **b)** comparison and coefficient of correlation for the peak points. **c)** normalized engineering stress-time response of the experimental fatigue test simulation for different materials. Pink curve represents a visco-hyperelastic material including continuous damage, yellow curve represents a visco-hyperelastic material and blue curve an hyperelastic material including continuous damage.

Table 1 -

Summary of the testing protocols.

Procedure 1: Uniaxial Tensile Tests (N=3) ▪ Uniaxial Tension in the y-direction up to failure: displacement control, rate 0.1mm/s
Procedure 2: Relaxation and Fatigue Tests (N=13) ▪ Stress relaxation in the y-direction at 35% failure displacement: rate 10mm/s stretch, 1000s holding ▪ Rest 20 min in the initial position ▪ Preload 0.7N ▪ Uniaxial tension in the y-direction up to 60% failure displacement, unload to 45% failure displacement: displacement control, 60 cycles, rate 0.1mm/s

Table 2 -

Constitutive model parameters obtain from the micro-genetic algorithm optimization.

Hyperelastic Parameters	Viscoelastic Parameters	Continuous Damage Parameters
C_{10} = 0.14 MPa	$\beta_{m,f1}$ = 5.08 (−)	$D_{max\ m}$ = 0.9 (−)
k_1 = 0.05 MPa	$\tau_{m,f1}$ = 33.59 s	$\Xi^{acc}_{max\ m} = 4.07$ MPa
k_2 = 0.23 (−)	$\beta_{m,f2}$ = 0.79(−) $\tau_{m,f2}$ = 44.14 s	C_m = 1.65 (−) $D_{max\ f}$ = 1.0 (−) $\Xi^{acc}_{max\ f} = 2.25$MPa C_f = 0.27 (−)